



In-depth mineralogical quantification of MSWI bottom ash phases and their association with potentially toxic elements

Qadeer Alam^{a,*}, Katrin Schollbach^{a,*}, Corrie van Hoek^b, Sieger van der Laan^b, Tom de Wolf^a, H.J.H. Brouwers^a

^a Department of the Built Environment, Eindhoven University of Technology, P.O. Box 513, 5600 MB Eindhoven, the Netherlands

^b Tata Steel, R&D, Microstructure & Surface Characterization (MSC), P.O. Box 10.000, 1970 CA IJmuiden, the Netherlands

ARTICLE INFO

Article history:

Received 1 September 2018

Revised 17 January 2019

Accepted 21 January 2019

Keywords:

MSWI

Bottom ash

Sequential extraction

Heavy metals

Mineralogy

ABSTRACT

Municipal solid waste incineration bottom ash fractions ≤ 4 mm are the most contaminated ones in terms of potentially toxic elements (PTEs). In order to estimate potential environmental impacts, it is important to understand the association of the PTEs with the mineral phases. Large area phase mapping (SEM/EDX) using “PhAse Recognition and Characterization - PARC” software in combination with quantitative X-ray powder diffraction has been used to characterize amorphous and crystalline BA phases for the first time. The results show that one of the main incineration products was melilite and an amorphous phase with a melilite composition. The ratio of crystalline to amorphous melilite was 1:2. They formed an inhomogeneous layer around BA particles and contained a high percentage of the PTEs, i.e., Cu, Zn, Ni and Cr. Other major sources of PTEs (especially Ni and Cu) were iron oxides produced during incineration and the weathering products, such as calcite and ettringite (Cu and Zn). After extensive characterization of BA, a sequential extraction procedure (SEP) was performed, which exposed bottom ash to different chemical environments designed to dissolve specific phases and release their PTEs into solution. The extracted solutions and solid residues generated from the extraction procedure were analyzed to identify the association between PTEs and dissolved phases of BA. By combining SEP results with information obtained via large area phase mapping it is shown that SEP can be used for studying the association of PTEs with the phase that cannot be investigated with XRD/EDX, such as organic matter and Fe-Mn-hydrous oxides. Furthermore, according to SEP results a high percentage (40–80 wt%) of each investigated PTE can be considered immobile and not susceptible to leaching in the environment.

© 2019 Elsevier Ltd. All rights reserved.

1. Introduction

In order to maximize the utilization of secondary raw materials such as ashes from thermal processes, several legislations and policies are being implemented across the European Union (EU Commission, 2014; Soil Quality Decree, 2007). Bottom ash (BA) is one of the major by-products obtained during municipal solid waste incineration (MSWI) in waste-to-energy plants (Landsberger et al., 1993). BA has been recycled to develop adsorbents (Chiang et al., 2014), mesoporous silica (Alam et al., 2018), zeolites (Penilla et al., 2003), ceramics (Bourtsalas et al., 2015) and building materials (Caprai et al., 2017). A recent Dutch initiative (Greendead-GD076, 2012) restricts the use of BA in protective applications that require periodic monitoring and sets the ambi-

tious target of recycling 100% of BA by 2020. However, the reuse of the BA is hindered by the presence of potentially toxic elements that can leach into the environment.

BA is a complex inorganic mixture containing melt products, glass, ceramics, unburned organic matter, silicates and metallic components (Bayuseno and Schmahl, 2010; Chimenos et al., 2000; Eusden et al., 1999; Speiser et al., 2001; Zevenbergen et al., 1994). The heterogeneous mix is formed during incineration when the material is burned to at least 850–1000 °C, followed by quenching in water in case of wet-discharge (Directive (2000)/76/EC, (2000)). Due to recent improvements in treatment technologies, a significant portion of BA can be recycled and used in different applications. However, BA fractions below 4 mm are usually separated because they are highly contaminated with PTEs e.g., Pb, Zn, Cu, Cr, Sb, Mo (Chimenos et al., 1999) and inorganic salts, e.g., chlorides and sulfates (Chen and Chiou, 2007). The leaching characteristics of BA as a function of particle size were investigated extensively and it is established that the BA fractions

* Corresponding authors.

E-mail addresses: q.alam@tue.nl (Q. Alam), k.schollbach@tue.nl (K. Schollbach).

¹ Both authors contributed equally.

(≤ 4 mm) are the most contaminated ones (Wiles, 1996). However, there is little information regarding the phase composition of the smaller size fraction of BA and their potential for retaining/releasing the contaminants is not clearly understood. This is especially true for the amorphous content of BA that is rarely quantified or analyzed with regard to chemical composition. It is, however, an important factor to take into account, since the amorphous content is at least partially made up of amorphous slag formed during the quenching and a potential source for PTEs. Due to the abundance of contaminants in this fraction of BA, it is crucial to understand its complete phase chemistry (crystalline and amorphous) and PTEs associated with it.

Generally, the PTEs such as Cu and Sn in BA are considered to be in oxide form because of the prevalent oxidative environment during the incineration process (Arickx et al., 2008; Wei et al., 2011). However, the high leaching potential of the BA fraction (≤ 4 mm) cannot be fully explained only on the basis of oxides. Additionally, the role of mineral constituents that can incorporate or adsorb PTEs is often overlooked during leaching and speciation studies (Cornelis et al., 2005; Piantone et al., 2004; Van Caneghem et al., 2016). Therefore, it is important to investigate the association of PTEs with BA phases by combining microanalysis and indirect experimental methods such as sequential extraction procedures (SEPs). Few studies have applied SEPs to determine the association of PTEs in BA by examining the extraction solution generated through the dissolution of targeted mineral phases (Bruder-Hubscher et al., 2002; Yao et al., 2012; Yao et al., 2010). SEP works by creating different chemical environments (Nirel and Morel, 1990) under which specific mineral phases are dissolved to determine PTEs associated with them. However, the changes in the mineral composition of the residues after the extraction are rarely investigated to confirm the association of PTEs with the targeted phases.

The heterogeneous mineralogy of BA and the association of PTEs with specific phases is challenging to investigate. Therefore, a novel multi-method approach consisting of energy dispersive x-ray spectroscopy (EDX) large area phase mapping (Schollbach et al., 2016; van Hoek et al., 2016) and quantitative X-Ray diffraction (XRD) was used for the identification and quantification of BA phases (both crystalline and amorphous). The spectral imaging (SI) dataset was subsequently analyzed using the software PARC (PhAse Recognition, and Characterization) to determine phase composition and spatial distribution for the first time. Moreover, to assess the association of the contaminants with specific phases, SEP was performed using the BCR protocol (Rauret et al., 1999). After every selective dissolution step, the extraction solutions and solid residues were analyzed. The analysis of the extracted solution, as well as the quantification of mineral changes after every step of SEP provides information about the phases that dissolved during the extraction and the PTEs released in the solution. The SEP data combined with spectroscopic methods validate the association of the PTEs with the mineral phases present in the ≤ 4 mm fraction of waste incineration BA.

2. Experimental section

2.1. Materials

MSWI bottom ash with a particle size below 4 mm was provided by Heros Sluiskil, the Netherlands. This stream was separated from the BA because of its high content of PTEs. Prior to separation of this fraction, the BA was water quenched and then weathered for 6 weeks at the plant site without removing ferrous and non-ferrous metals. On the basis of our previous investigation, the BA (≤ 4 mm fraction) was separated into three different fractions, namely, S (≤ 0.125 mm), M (0.125–1 mm) and L (1–4 mm) (Alam et al., 2017). The size distribution has been reported

elsewhere (Alam et al., 2016). Before sieving, the material was dried at 105 °C until constant weight.

2.2. Mineralogical and chemical analyses

Chemical analysis of all three BA fractions was carried out with X-ray fluorescence spectrometry (XRF; PANalytical Epsilon 3, standardless) using fused beads. Total organic content (TOC) was measured with the Behr CS30HT Coulometric carbon/sulfur analyzer at 550 °C. XRD measurements for the untreated and size-separated BA fractions were performed with a Bruker D4 equipped with a LynxEye detector. All other samples were measured using a PANalytical X'Pert Pro with an X'Celerator detector. Both devices had fixed divergence slits with an opening of 0.5° and 0.04 rad soller slits. The range of 5–120° 2Theta was measured with Co-Tubes ($K\alpha_1$ 1.7901 Å, $K\alpha_2$ 1.7929 Å). A step size of 0.02 was used with both devices. Phase identification was carried out with X'Pert HighScore Plus 2.2 (PANalytical) using the ICDD PDF-2 database, while the quantification itself was done with TOPAS 4.2 (Coelho, 2018). The crystal structures for the quantification were taken from the ICSD database (FIZ Karlsruhe). Prior to measurements, samples were milled below 10 μ m. In all cases, 10 wt% of Si was added to the original samples as an internal standard for the quantification of the amorphous content (Gualtieri, 2000).

Quantitative Rietveld analysis was performed on the three BA fractions S, M and L that were separated from the original below 4 mm BA fraction. Since both M and L showed very similar composition and behavior during SEP, only S and M will be discussed further. Additionally, the quartz content of the BA fractions was determined independently using DSC (Mettler Toledo; DSC822e) and used as an internal control for Rietveld quantification. The thermal transition for α - β inversion of quartz at 573 °C was measured with a heating and cooling rate of 10 °C min⁻¹. After two cycles of heating between 500 and 600 °C, the cooling peak was used for quantification (Hendrix et al., 2017). The quartz content measured via DSC was 15 wt% for the M fraction and 7 wt% for the S fraction, which was in good agreement with the values determined via Rietveld quantification if the general inhomogeneity of BA is taken into account. The quartz contents in the S and M fractions determined via quantitative XRD were 15.7 and 6.6 wt%, respectively. In subsequent SEP steps, quartz becomes enriched in the residue due to the dissolution of other phases. However, it can be assumed that the original quartz contents in the S and M fractions remained unchanged because it is not reactive under the SEP conditions. The quantification results were scaled accordingly to the constant quartz content.

Scanning electron microscopy (SEM) measurements combined with X-Ray microanalysis (EDX) were performed on the original BA (below 4 mm) fraction. The sample was prepared by mounting it in epoxy (Struers EpoFix) and polished to a flat surface without the use of water. It was then coated with about 10 nm of carbon. The spectral imaging (SI) data sets were acquired for the PARC analysis using a JEOL JSM-7001F SEM equipped with two 30 mm² SDD detectors (Thermo Fisher Scientific) and NORAN-System7 hardware with NSS3.3 software. The SEM accelerating voltage was 15 kV, the beam current 6.2 nA and the step size of the measurement 1 μ m. The SIs were acquired for a total of 402 SEM image fields. Each field contained 512 \times 382 data points with a total measuring area of 5.5 \times 3.5 cm². The PARC software enables the grouping of elemental spectra taken from each measured pixel with EDX according to elemental peaks above a predefined threshold and its mutual ratio (Fig. 1). These groups can then be represented as color-coded phase maps (van Hoek et al., 2016). From PARC analysis thirty-six different phases were identified, of those, only phases above 0.3 area% were further analyzed. They were twenty in total and accounted for 98.2% of the area measured. The area% can be

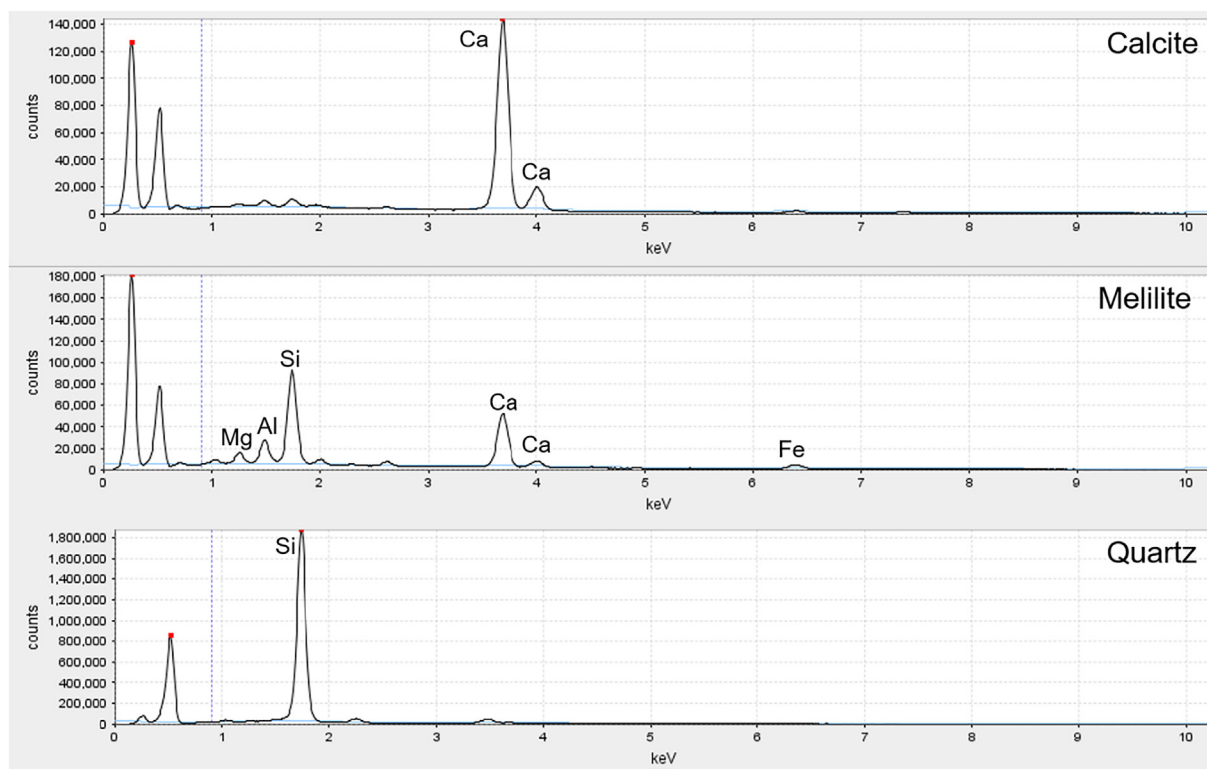


Fig. 1. Examples of a cumulative EDX spectrum of calcite, melilite and quartz phase from MSWI bottom ash generated with PARC.

recalculated to wt% using the density of the mineral phases. For the phases that could not be identified, an average raw density of 2.9 g/cm³ was used that is the reported density for melilite (Teichert et al., 1982). This value was chosen because melilite-like phases made up a significant part of the unidentified phases as discussed in Section 3.1.

The column-leaching test was performed to assess the leaching of PTEs from BA in accordance with NEN 7383:2004. The contents of chlorides and sulfates in the leachates were determined with high performance liquid chromatography (HPLC) according to NEN-EN-ISO 10304-1.

2.3. Sequential extraction procedure

Sequential extractions protocols were designed for determining the PTEs contents of different phases making up the soil and sediments that generally present a lower acid buffering capacity as compared to alkaline residues. In this study, a standardized extraction procedure that is BCR (the Community Bureau of Reference, now the European Union 'Measurement and Testing Programme') was selected (Rauret et al., 1999) and combined with several complementary analytical methods (SEM, PARC and XRD) to study the association of PTEs with the BA phases. Moreover, BCR sequential extraction protocol find application in other materials, such as incineration ashes (Yu et al., 2013) and mine tailings (Davidson et al., 2005). The specificity of BCR in term of targeting the intended phase can be assessed by using a combination of the analytical methods after each extraction step.

SEP was performed on size-separated fractions of BA. The reagents (analytical grade from Sigma-Aldrich) used in each step and phases that were expected to dissolve, in parenthesis, are as follows:

1. Exchangeable ions and acid extractable phases (carbonates): 160 ml of 0.11 M acetic acid (HOAc, pH = 2.85) was added to 4 g of BA. The resulting mixture was left shaking at 40 rpm overnight, at room temperature. Afterwards, the supernatant was separated by centrifugation at 3000g for 20 min. The residue from the extraction was washed with 20 ml MiliQ water by shaking for 15 min and separation by centrifugation.
2. Reducible phases (Fe-Mn-oxyhydroxides): The residue from the previous extraction step was mixed with 160 ml of 0.5 M hydroxylammonium chloride solution (acidified with 2 M HNO₃). Subsequently, after the extraction, solid residues were separated and washed according to the procedure specified in step 1.
3. Oxidizable phases (sulfides, organic matter): Hydrogen peroxide (40 ml, 8.8 M) was added in small aliquot to the residue from the second step and the mixture was left for 1 h at room temperature. Later, the same mixture (in a loosely capped bottle) was digested at 85 °C and after 1 h sample heated to near dryness. This digestion was performed twice. Subsequently, 200 ml of ammonium acetate (pH was adjusted to 2.0 by adding HNO₃) were added to the residue. Afterwards, extraction and separation were performed with the same procedure described in step 1.
4. Residual (silicates, well-crystallized oxides): The residue from the previous extraction was digested with aqua regia according to the ISO 11466 protocol. Additionally, aqua regia extraction was performed on original size-separated fractions of BA to obtain the pseudo-total content of PTEs.

The supernatants from the extraction steps were filtered (0.2 µm PTFE filter) and acidified with 0.2% (v/v) of 15 M HNO₃. These extraction solutions were analyzed with either inductively coupled plasma-optical emission (ICP-OES; Varian 730-ES) or flame-atomic absorption spectroscopy (FAAS; Thermo Scientific

ICE 3000 series). All extractions were performed four times and the contents of PTEs were normalized to the dry mass of BA and presented in ppm. The solid residues from the extraction steps were dried at 60 °C for the duration of 48 h to minimize the changes in mineral composition due to the drying.

3. Results and discussion

3.1. Mineralogy of MSWI bottom ash

In order to arrive at a concise mineralogical description of the BA, the phase quantification from PARC (Table 1) was combined with the results from XRD-Rietveld analysis (Table 2). The PARC method was used to identify the phases present in BA (≤ 4 mm), their quantities as well as their average chemical compositions. The results pertain to both the M and S fractions. The PARC phases were then assigned to minerals based on chemical composition and information obtained by XRD. If they could not be identified then a name was given based on their composition using cement notation (Table 1). They were most likely amorphous in nature or present in very small amounts that were not detectable via XRD.

XRD analysis showed the presence of mineral phases that were not visible in PARC. Among them were the sulfate-containing phases ettringite and gypsum (Table 2), which are weathering products of BA (Eusden et al., 1999). They were not visible in PARC as individual phases likely due to their small particle size. The EDX resolution is inherently limited at 15 kV to about 1 μ m. However, the local phase environment for SO_3 was identified with PARC, because the phases CA-S and the CA-S contained 23.8 and 17.2 wt% of SO_3 (Table 1), respectively. This SO_3 content most likely originated from gypsum and ettringite embedded in these phases. Ettringite has been observed in BA before (e.g., Alam et al., 2017) and forms in the presence of gypsum and reactive aluminum at high pH (Hampsoim and Bailey, 1982).

In general, PARC gave a good overview of the chemical heterogeneity of BA as shown in Fig. 2. Most grains consisted of a relatively homogenous core surrounded by an inhomogeneous layer containing smaller particles (Figs. 2 and 3a). This layer was the result of the incineration process that creates slag, which coats bigger particles and binds smaller particles together (Fig. 2, area C3). This layer along with BA particles was subjected to water quenching and was further modified during the weathering. Based on the PARC results, this layer appeared to be mostly comprised of melilite (14.1 area%) and the phases CAS 1 (5.6 area%) and CAS 2 (2.7 area%), which were also close to melilite in composition.

Overall melilite was the predominant PARC phase (14.1 area%; 13.1 wt%) in the sample. Its presence was confirmed via XRD-Rietveld analysis, albeit in a much smaller amount (4.7 wt%). The difference was likely due to the fact that with PARC both amorphous and crystalline melilite phases were recognized (but not distinguished), while XRD only detects the crystalline form. Melilites are a group of minerals that form solid solutions with several end members and can incorporate a large number of different PTEs in their crystal structure (Deer et al., 1986) (Table 3). The most important end members in the group are akermanite ($\text{Ca}_2\text{MgSi}_2\text{O}_7$) and gehlenite ($\text{Ca}_2\text{Al}_2\text{SiO}_7$). Melilites crystallize out of the alkaline Ca-rich melt that is produced during incineration of MSWI (Eighmy et al., 1994). Fig. 3c shows the SEM image of melilite that crystallized together with spinel. Due to the rapid quenching after incineration part of the melt also forms amorphous phases with a melilite like composition. Although in a pure $\text{CaO-MgO-Al}_2\text{O}_3\text{-SiO}_2$ system temperature of at least 1385 °C are necessary for melilite formation (Osborn and Schairer, 1941), the temperature inside an MSW incinerator is generally only around 850–1000 °C with localized variations. The difference can be explained by the incor-

Table 1
The average chemical composition and amount (area%) of phases identified in the BA fraction (≤ 4 mm) with the PARC analysis.

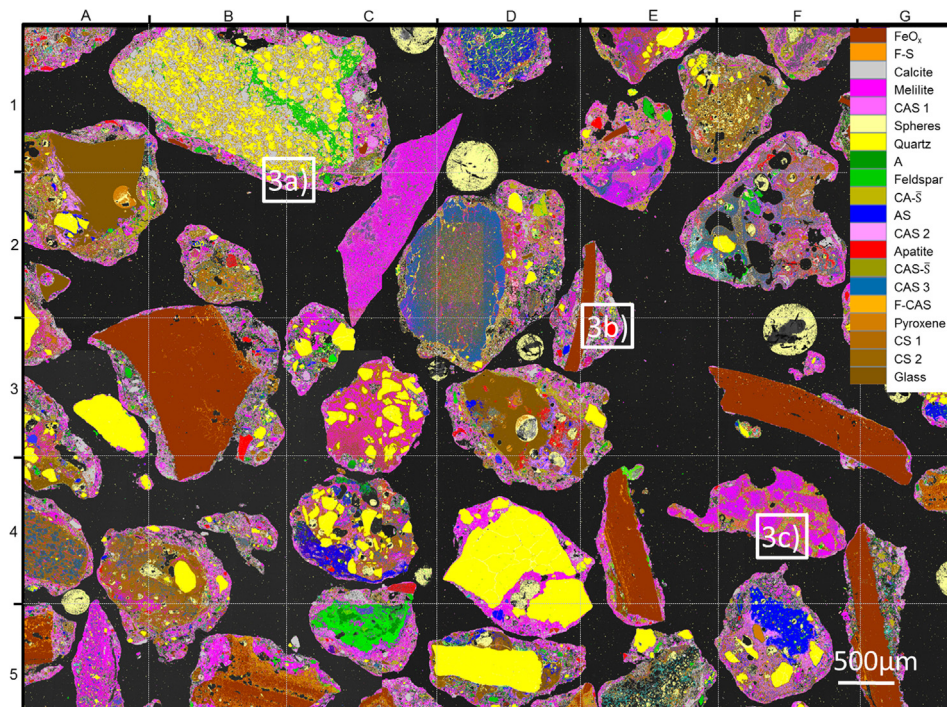
Oxides	FeOx	Calcite ¹	Melilite	Quartz	Feldspar	Apatite	Diopside	Glass	S ²	CAS 1	CAS 2	CAS 3	CAS-SO ₄	F-CAS	CS 1	CS 2	FS	A	CA-SO ₄	AS
Na ₂ O	0.43	1.75	2.36	0.54	2.69	3.33	5.03	6.80	2.07	2.28	6.86	2.10	2.20	1.19	2.05	2.85	1.38	2.79	2.14	8.54
MgO	0.38	1.22	2.40	0.38	2.46	1.50	8.48	3.51	1.37	1.76	1.86	9.79	1.31	1.56	3.19	3.49	0.85	2.24	1.02	1.46
Al ₂ O ₃	1.32	6.90	18.05	0.87	24.91	3.02	5.39	3.72	5.15	20.14	18.38	15.40	12.30	10.28	3.41	7.56	2.82	43.61	16.65	20.85
SiO ₂	1.87	6.75	28.44	94.34	43.76	9.92	47.93	62.45	68.16	10.52	37.38	32.97	17.07	11.76	42.52	30.18	14.94	12.54	5.63	51.19
P ₂ O ₅	0.13	1.47	1.50	0.10	0.99	26.74	1.09	0.72	1.33	1.52	1.37	1.19	1.52	0.62	0.92	1.78	0.46	1.18	0.76	0.87
SO ₃	0.48	5.63	3.15	0.90	2.10	1.82	0.84	0.70	1.42	8.66	1.54	1.07	17.18	0.82	0.42	2.57	0.25	4.60	23.77	0.83
Cl	0.24	1.69	1.28	0.10	1.51	1.43	1.01	0.53	1.51	2.56	0.93	1.17	2.18	0.44	0.35	1.62	0.24	3.09	2.47	0.73
K ₂ O	0.08	0.39	1.03	0.16	2.64	0.45	1.26	1.37	0.77	0.69	2.00	0.75	1.01	0.26	0.30	0.85	0.31	0.92	0.77	3.40
CaO	2.33	66.87	33.16	0.64	11.14	46.32	18.10	14.32	9.58	45.20	21.85	27.10	36.72	12.02	38.99	37.80	4.47	18.67	41.01	6.89
TiO ₂	0.35	1.53	1.27	0.07	0.98	0.88	1.00	0.58	0.70	1.24	1.14	1.07	1.01	1.53	1.25	1.68	1.09	1.10	0.74	1.25
V ₂ O ₅	0.06	0.02	0.01	0.04	0.05	0.05	0.08	0.04	0.02	0.03	0.01	0.07	0.09	0.06	0.06	0.03	0.11	0.06	0.14	0.01
Cr ₂ O ₃	0.07	0.09	0.16	0.05	0.11	0.16	0.24	0.23	0.10	0.11	0.18	0.22	0.24	0.28	0.52	0.24	0.19	0.22	0.11	0.08
MnO	0.22	0.41	0.07	0.03	0.10	0.04	0.30	0.11	0.07	0.08	0.06	0.07	0.11	0.30	0.25	0.18	0.31	0.14	0.06	0.05
Fe ₂ O ₃	91.18	3.44	5.85	1.00	4.38	2.56	6.66	3.72	6.12	3.18	4.67	5.09	4.25	57.21	4.60	7.14	70.58	5.40	2.25	1.96
NiO	0.13	0.26	0.09	0.07	0.08	0.27	0.25	0.05	0.05	0.10	0.05	0.09	0.22	0.14	0.24	0.10	0.20	0.15	0.14	0.04
Cu ₂ O	0.26	0.25	0.19	0.07	0.30	0.24	0.44	0.20	0.37	0.26	0.14	0.27	0.35	0.55	0.13	0.28	0.63	0.38	0.42	0.14
ZnO	0.30	0.45	0.51	0.11	0.72	0.39	0.99	0.31	0.40	0.75	0.77	0.68	0.56	0.51	0.47	0.64	0.61	1.11	0.54	1.07
MoO ₃	0.19	0.88	0.50	0.53	1.12	0.90	0.89	0.64	0.81	0.91	0.79	0.90	1.69	0.48	0.33	1.00	0.57	1.80	1.38	0.64
Amount (area%)	12.2	8.8	14.1	12.6	3.5	1.6	1.2	5.1	7.0	5.7	2.7	4.2	0.7	0.7	3.4	7.8	0.7	2.3	2.3	3.3

¹ The PARC phases were then assigned to minerals based on chemical composition and information obtained with XRD.

² If the phase could not be identified it was given a name based on its composition using cement notation. These phases were most likely amorphous in nature or present in very small amounts not detectable via XRD.

Table 2Comparison between the phase quantification of the original ≤ 4 mm BA fraction determined via PARC and XRD (weighted average of the S, M and L fraction).

Phases	PARC average (area%)	PARC average (wt%)	Density (g/cm ³)	Rietveld average (wt%)
Melilite	14.1	13.1	2.9	4.7
Plagioclase	3.5	2.9	2.6	5.7
Calcite	8.8	7.6	2.7	13.5
Zeolite	–	–	–	0.1
Pyroxene	1.2	1.3	3.5	4.2
Ettringite	–	–	–	0.2
Gypsum	–	–	–	0.2
Halite	–	–	–	0.8
Apatite	1.6	1.6	3.2	6.5
Quartz	12.6	10.7	2.7	12.5
Rutile	–	–	–	1.3
Hematite	–	–	–	3.8
Spinel	–	–	–	8.9
Wuestite	–	–	–	1.5
FeO _x ^a	12.2	20.3	5.2	14.2
Amorphous	45.9 ^b	42.5	2.9	36.1

^a Sum of Hematite, Magnetite and Wuestite for Rietveld results.^b Sum of remaining Phases for PARC results.**Fig. 2.** PARC result for the original below 4 mm BA fraction; this figure includes a grid reference for orientation using numbers (left side) and letters (top side). Markings in a box numbered as 3a–3c identify the areas of the SEM measurements shown in Fig. 3. Phases that could be identified as minerals were given the appropriate mineral name, the other phases were named based on their most common oxides using cement chemistry notation (C–CaO, S–SiO₂, A–Al₂O₃, F–Fe₂O₃, S–SO₃).

poration of sodium and iron that are known to reduce the melting temperatures drastically (Deer et al., 1986). This was confirmed by the composition of the melilite in the investigated BA, that was $(\text{Ca}_{1.7}\text{Na}_{0.23}\text{K}_{0.07})(\text{Al}_{0.55}\text{Fe}_{0.22}\text{Mg}_{0.18})(\text{Si}_{1.45}\text{Al}_{0.54})\text{O}_7$ based on PARC. The results of PARC analysis also indicated that a significant amount (i.e., 10–15% of the total content) of Cr, Ni, Cu, Zn was contained in melilite (Table 4).

The most common phases besides melilite in this BA were quartz (12.6 area%; 10.7 wt%) and calcite (8.8 area%; 7.6 wt%). Quartz is inert during incineration and mechanically resistant, so it was present as relatively large particles with clearly defined borders (Fig. 2, area D4). Quartz can be natural in origin since it is a common mineral on the earth's surface. It is also extensively used in building materials. Calcite is also a common industrial and nat-

ural mineral, as well as a weathering product of BA (Chimenos et al., 2000). Larger particles of calcite as part of natural sandstone could be seen in Fig. 2 (area B1) and Fig. 3a, which indicate the variable temperature during incineration leading to incomplete calcination. In addition to that, smaller grains of calcite were observed dispersed throughout the sample that were a product of weathering reactions (Fig. 2, area A3 and A4). The amount of calcite detected via Rietveld-analysis was much higher (13.5 wt%) possibly due to the presence of many calcite grains smaller than 1 μm that were formed during weathering. Calcite is able to incorporate a number of PTEs in its crystal structure (Table 3) and based on PARC data it was associated with Ni in particular (Tables 1 and 4). Studies showed that this metal can be incorporated into the crystal structure of calcite (Lakshatanov and Stipp, 2007).

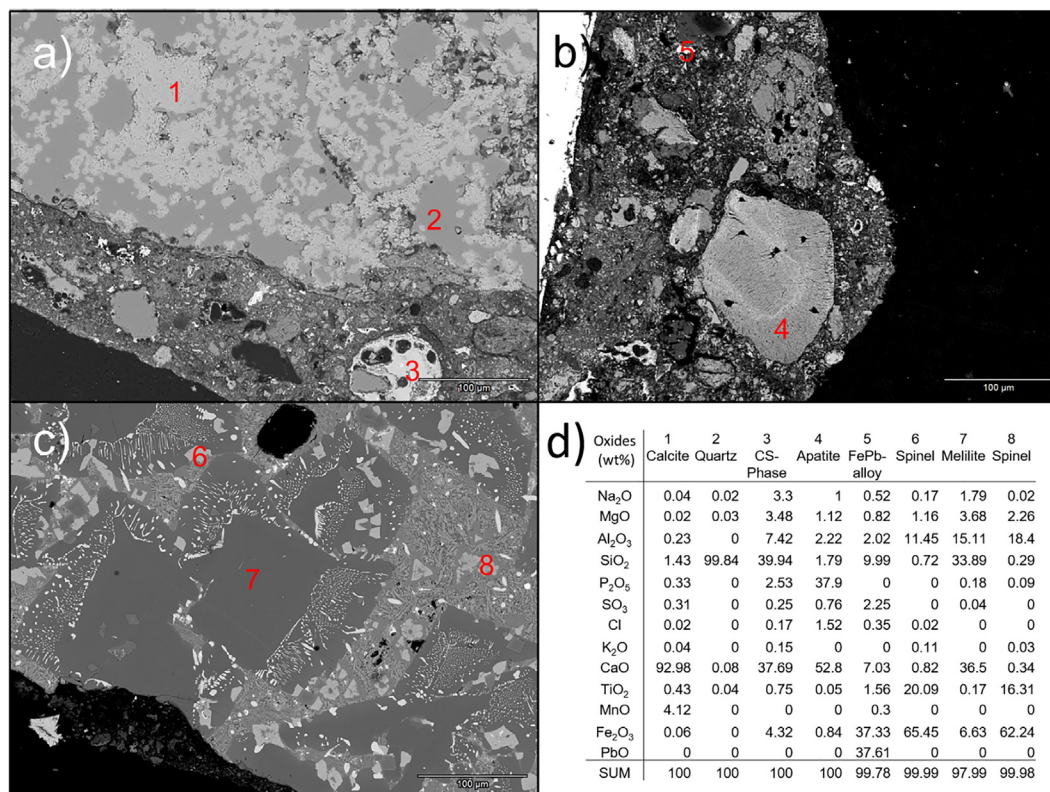


Fig. 3. SEM micrographs of BA particles showing (a) a natural piece of sandstone surrounded by incineration residue. (b) piece of apatite embedded in incineration residue (c) mix of spinel and melilite (d) chemical composition of the points analyzed with EDX: 1 – calcite, 2 – quartz, 3 – CS phase, 4 – apatite, 5 – FePb alloy, 6 – spinel, 7 – melilite, 8 – spinel.

Another mineral group present in BA were the iron oxides, i.e., hematite, magnetite, and wuestite that could not be differentiated using PARC, only via XRD. They were labeled together as FeO_x and made up 12 area% (Fig. 2, area F3) or 20.3 wt% due to their high density. While iron oxides occur naturally, their origin in BA is primarily from the metallic scrap iron (Fe⁰) present in MSW and the FeO_x are produced during incineration (Wei et al., 2017). Magnetite is part of the spinel mineral group that can have a highly variable composition that may include many PTEs, while hematite can also incorporate Al, Ti or Ni (Table 3). In fact, the FeO_x phase contained 22.1 wt% of Ni and 22.1 wt% Cu that likely originated from the Fe⁰ (Table 1). Different iron hydroxides can also be present in BA (Dijkstra et al., 2006; Meima and Comans, 1998) but they tend to be of low crystallinity with small particle sizes making detection with PARC or XRD unlikely (Bigham and Nordstrom, 2000).

Two other phases could only be identified via PARC. One was present as round, porous spheres (named S in Table 1) similar to fly ash particles (Fig. 2, area F3 and C1) (7 area%). These spheres had a silica content of around 68 wt% and likely represent incineration residues of rubber or plastics containing silica as a filler. The other phase was industrially produced glass (soda-lime glass) with 5.1 area% (Fig. 2, area A2). It was easily distinguishable by its homogenous composition and microstructure. The glass particles locally show edges that were partially reacted, while others were unreacted, illustrating the temperature variations during the incineration process.

Feldspar with a plagioclase composition (3.5 area%) and pyroxene (1.1 area%) were also present in smaller quantities and identified via both PARC and XRD. They are both common natural minerals and potential incineration products (Eighmy et al., 1994). Pyroxenes and diopside (MgCaSi₂O₆) in particular, are known to occur together with melilites in alkaline Ca-rich melts

(Deer et al., 1986). Pyroxene is known to incorporate appreciable amounts of PTEs (Deer et al., 1997) (Table 3) and had a nominal composition of (Ca_{0.77}Na_{0.41})(Mg_{0.53}Fe_{0.21}Al_{0.26})Si_{1.99}O₆ based on PARC data. The presence of pyroxene with a diopside structure was also confirmed by XRD measurements. Furthermore, apatite was present in 1.6 area%. A particle of it can be seen in Fig. 3b. Based on its microstructure, it did not form during the incineration or weathering but possibly originated from animal or fish bones that were part of the MSW feed (Palmer et al., 2008).

The overall quantitative composition of the BA fractions S (≤0.125 mm) and M (0.125–1 mm) determined by the Rietveld method is given in Figs. 4 and 5. The phase composition for the L fraction (1–4 mm) is provided in Appendix A (Fig. A2). The main difference between the S and M fraction was the presence of ettringite (4.1 wt%), gypsum (5.4 wt%) and a chabazite type (CHA) zeolite (2.1 wt%), which were only present in the S fraction. These are the weathering products formed from the layer of slag that covers the BA particles and are easily separated from bigger grains during transport and sieving due to their low mechanical resistance and brittle nature. The weathering phases tend to accumulate in the S fraction, increasing the calcite content. Quartz showed the opposite behavior, the S fraction contained 6.6 wt%, while the M fraction contained 15.7 wt% of quartz. The iron oxides showed the same behavior as quartz in the S and M fractions; they contained 6 and 13.3 wt%, respectively. The amorphous content of the two fractions was very similar, 34.9 wt% for the S and 34.2 wt% for the M fraction.

3.2. Comparison of PARC and XRF

In order to evaluate the internal consistency of the PARC data, the data was used to calculate the bulk chemical composition of

Table 3

Mineral phases identified via XRD in the BA along with the ICSD number of the crystal structure used for the Rietveld refinement. The chemical formula, source and ions that can be incorporated in the crystal structure of the minerals are also given (chemical species in bold are most frequently found).

Mineral	Formula	Substitution	Source
Apatite (1707)	X_5YTi_3	X = Ca , K, Na, Mn, Ni, Cu, Co, Zn, Pb, Sb Y = OH ⁻ , F ⁻ , Cl ⁻ T = PO₄³⁻ , CO ₃ ²⁻ , SO ₄ ²⁻ , SiO ₄ ⁴⁻ AsO ₄ ³⁻ (Hughes and Rakovan, 2002)	Bone material from vertebrates and fish
Calcite (20179)	CaCO ₃	X = Ca , Mg ²⁺ , Fe ²⁺ , Sr ²⁺ , Mn ²⁺ , Ba ²⁺ , Cd ²⁺ , Zn ²⁺ , Cu ²⁺ , Co ²⁺ , Ni ²⁺ (Lakshatanov and Stipp, 2007; Railsback, 1999)	Weathering product
Cristobalite (153886)	SiO ₂		Metastable, used as filler in plastics and ceramics, inert ¹
Corundum (92628)	Al ₂ O ₃		Common in paints and coatings, inert ¹
Ettringite (251756)	X ₆ [Y ₂ (OH) ₁₂ ·24 H ₂ O] [T ₃ ·nH ₂ O]	X = Ca²⁺ , Cu ²⁺ , Co ²⁺ , Ni ²⁺ , Pb ²⁺ , Na ⁺ Y = Al³⁺ , Si⁴⁺ , Fe ³⁺ , Cr ³⁺ , Mn ⁴⁺ , Ti ⁴⁺ T = SO₄²⁻ , OH ⁻ , Cl ⁻ , CrO ₄ ²⁻ , SiO ₄ ⁴⁻ (Gougar et al., 1996)	Weathering product
Gypsum (27875)	CaSO ₄ ·2H ₂ O		Weathering product
Halite (240598)	NaCl		Incineration/weathering product
Hematite (56372)	X ₂ O ₃	X = Fe³⁺ , Al ³⁺ , Ti, Ni ²⁺	Incineration product
Melilite (7697)	X ₂ Y(T ₂ O ₇)	X = Ca²⁺ , Na⁺ , K ⁺ , Sr ²⁺ , Ba ²⁺ Y = Al³⁺ , Fe^{2+/3+} , Mg²⁺ , Si⁴⁺ , Co, Cu, Zn, Mn ²⁺ T = Si⁴⁺ , Al ³⁺ , Fe ³⁺ (Pöllmann, 2010; Wiedenmann et al., 2009)	Incineration product
Plagioclase (87656)	XY ₄ O ₈	X = Na⁺ , Ca²⁺ , K⁺ , Ba ²⁺ Y = Si⁴⁺ , Al³⁺ (Carpenter, 1994)	Incineration product, common natural mineral
Pyroxene (64978)	XYT ₂ O ₆	X = Fe^{2+/3+} , Mg²⁺ , Al ³⁺ , Cr ³⁺ , Ti ^{3+/4+} , Mn ²⁺ , Zn ²⁺ , Ni ²⁺ Y = Ca²⁺ , Na⁺ , Mg²⁺ , Mn ²⁺ , Na ⁺ , Li ⁺ T = Si³⁺ , Al³⁺ , Fe ³⁺ (Deer et al., 1986)	Incineration product, common natural mineral
Quartz (93974)	SiO ₂		Common natural and industrial mineral, inert ¹
Rutile (74532)	TiO ₂		Common in paints and coatings, inert ¹
Spinel (98087)	XY ₂ O ₄	X = Fe^{2+/3+} , Mg²⁺ , Zn ²⁺ , Mn ²⁺ , Ni ²⁺ , Cu ²⁺ , Pb ²⁺ , Co ²⁺ , Cd ²⁺ Y = Al³⁺ , Fe³⁺ , Cr ³⁺	Incineration product
Wuestite (27237)	FeO		Incineration product
Zeolite (34172)	X(AlO ₂) _n (SiO ₂) _{1-n} ·mH ₂ O	X = Ca²⁺ , K⁺ , Na⁺ , Ba ²⁺ , Sr ²⁺	Weathering product

¹ Not affected by the MSWI conditions.

the BA sample and the results were compared to XRF results (Table 5). XRF results for each individual fraction are provided in Appendix A (Table A1).

In general, the bulk chemical composition calculated from the PARC data and the one obtained via XRF were in good agreement. Due to the high heterogeneity of the BA, some variation in the results was expected, especially since the area that could be measured with PARC was limited. The biggest differences between the PARC and XRF results were noted for the SiO₂ content (8.6 wt%) and Fe₂O₃ (7.7 wt%) as shown in Table 5. The PARC analysis showed that both quartz and the iron oxides present in BA form larger particles due to their mechanical resistance. They were therefore particularly susceptible to statistical variation which explains the discrepancy. The XRF measurements were also done using fused beads, which accounts for lower amounts of Na₂O, Cl and SO₃. The Sb₂O₃ content could not be measured via PARC due to the overlap of the Sb L_α and the Ca K_α lines that were used for quantification.

The leaching of PTEs and other contaminants from the original BA (≤4 mm) obtained using a column test is provided in Table 6 along with the limits for the granular building material for use in the open environment (Soil Quality Decree, 2007). This fraction of BA contained a large number of leachable contaminants, however, only Cu, Mo and chlorides were above the limit. The contents of Zn, Ni, Cr, Pb and Sb were under the limit but previous studies (Alam et al., 2017, 2016) indicate that leaching of these elements commonly exceeds the limit for use in non-isolated applications.

3.3. SEP results

3.3.1. Exchangeable fraction (F1)

In the first step of SEP (F1), carbonates and acid soluble salts were the intended targets. The mineral composition of the solid residues S and M recovered from the F1 extraction step are denoted as S-F1 and M-F1 in Fig. 4a and b, respectively. The partial dissolution of the weathering phases, e.g., calcite, gypsum and zeolite was observed during F1. Moreover, ettringite is easily affected by changes in the physiochemical environment and was completely dissolved (Fig. 4a: bar S-F1). The incomplete decomposition of calcite that was observed in S can be attributed to the fact that the added acid was not sufficient to dissolve all of its initial calcite content. This indicates the inadequacy of the SEP BCR protocol (Rauret et al., 1999) while dealing with samples rich in carbonates, which was in line with the literature, where soils with high content of carbonates were studied with the BCR protocol (Sulkowski and Hirner, 2006). In addition to the targeted phases, small amounts of plagioclase, apatite, melilite and spinel were also dissolved. During F1, the amorphous contents of S and M increased by 2.9 and 9.1 wt%, respectively. It is likely that dissolution of the crystalline phases resulted in the formation of new amorphous phases.

The PTEs (Zn, Cu, Ni, Cr, Pb and Sb) released during the F1 extraction step for S and M are presented in Fig. 6a and b, respectively. The PTEs extracted from the L fraction during SEP are provided in Appendix A (Fig. A4). The concentration of PTEs extracted during F1 from the S fraction were Zn: 817, Cu: 76, Ni

Table 4
Percent distribution of PTEs (wt%) in the PARC phases from the BA fraction (≤ 4 mm), calculated based on the content of PTE in each mineral phase and their respective amount present in BA.

PTE	FeOx	Calcite	Melilite	Quartz	Feldspar	Apatite	Pyroxene	Glass	Spheres	CAS 1	CAS 2	CAS 3	CAS-SO ₄	F-CAS	CS 1	CS 2	FS	A	CA-S	AS	SUM
Cr	9.8	5.0	15.2	3.7	2.3	1.8	2.2	7.6	4.5	4.2	3.1	6.1	1.0	1.3	11.7	12.6	0.9	3.4	1.7	1.8	100
Ni	22.1	17.4	10.1	6.2	1.9	3.8	2.8	1.9	2.8	4.5	1.1	3.0	1.2	0.8	6.5	6.3	1.1	2.8	2.7	1.2	100
Cu	22.1	7.9	10.3	3.3	3.7	1.6	2.4	3.9	10.0	5.6	1.5	4.5	0.9	1.5	1.7	8.5	1.7	3.5	3.7	1.8	100
Zn	12.6	7.2	13.9	2.5	4.4	1.3	2.6	3.0	5.5	8.2	4.0	5.6	0.7	0.7	3.1	9.7	0.8	5.0	2.4	6.8	100

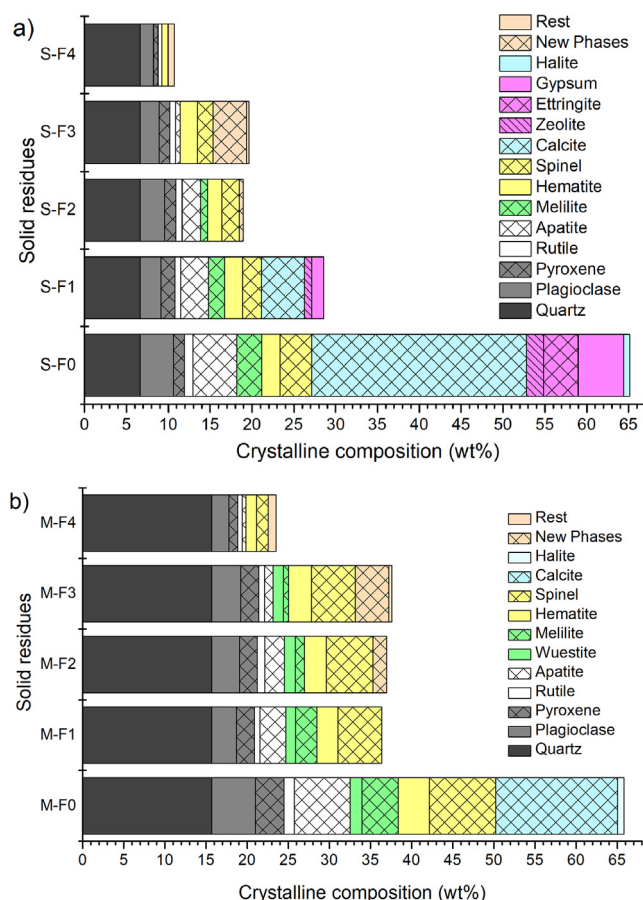


Fig. 4. The crystalline composition, determined via quantitative XRD, of the original bottom ash fractions and of the residues after each SEP step, (a) S fraction (≤ 0.125 mm) and (b) M fraction (0.125 – 1 mm). For example, S-F0 refers to the composition of the original S fraction and S-F1 to the residue of the small fraction after the first step F1 from SEP, etc. The amorphous content is not shown in the graph and can be found in Fig. 5.

and Cr: 4 ppm each. On the other hand, contents of PTEs in the supernatant from the M fraction were significantly higher, Zn: 1909, Cu: 269, Ni: 4 and Cr: 10 ppm. However, the opposite was expected due to the significantly higher absolute content of the PTEs (Fig. 6) and specific surface area of the S fraction. The higher content of PTEs from the M fraction can be explained by the respective amount of FeO_x phases (hematite, spinel and wuestite) that was present in the S and M fractions, 6 and 13.3 wt%, respectively. As explained earlier (Section 3.1.) FeO_x was more concentrated in the bigger size fractions of BA (fraction M) due to its mechanical resistance and contained the majority of Zn, Cu and Ni (Table 4), which led to the higher contents of these PTEs released from M.

Interestingly, in the F1 extraction solutions (initial pH 2.85) from both fractions, no antimony was detected. Although, anti-

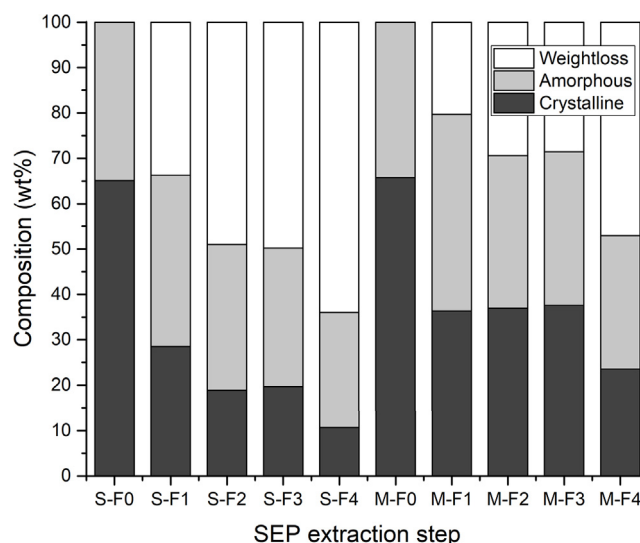


Fig. 5. The composition of the S (≤ 0.125 mm) and M (0.125 – 1 mm) fractions before SEP (S-F0 and M-F0) and after each SEP step. Mass loss was calculated based on the assumption that total quartz content remains unchanged.

Table 5

Comparison between the chemical compositions of the original BA ≤ 4 mm obtained from the PARC and XRF results. The total contents of PTEs released during SEP, (obtained by calculating the weighted average of PTEs released from S, M and L fraction) are also presented. All values given below are in wt%.

Oxides	PARC average	XRF average	PTE's average extracted via SEP
Na ₂ O ^a	2.3	0	–
MgO	2.0	2.38	–
Al ₂ O ₃	9.4	12.97	–
SiO ₂	32.8	41.36	–
P ₂ O ₅	1.3	1.73	–
SO ₃ ^a	2.7	1.24	–
Cl ^a	1.0	0.08	–
K ₂ O	0.7	1.16	–
CaO	22.3	20.99	–
TiO ₂	0.9	1.47	–
V ₂ O ₅	0.0	0.01	–
Cr ₂ O ₃	0.1	0.10	0.04
MnO	0.1	0.16	–
Fe ₂ O ₃	22.6	14.91	–
NiO	0.1	0.03	0.02
Cu ₂ O	0.2	0.36	0.73
ZnO	0.5	0.69	0.60
Sb ₂ O ₃ ^b	–	0.15	–
Rest	0.7	0.21	–

^a The differences in Na₂O, Cl and SO₃ are due to the preparation of XRF samples as fused beads.

^b Sb₂O₃ could not be determined with PARC because of the overlap of the Sb L_α and the Ca K_α lines.

mony from MSWI bottom ash is reported to be leachable at acidic pH (Verbinnen et al., 2014). Furthermore, the leaching analysis according to column leaching test showed the presence of leach-

Table 6

Leaching of potentially toxic elements, sulfates and halides from BA (≤ 4 mm) and comparison with the limits for granular construction material employed in non-isolated applications (Soil Quality Decree, 2007).

Parameters	Granular material ¹ [mg/kg]	BA (≤ 4 mm) ² [mg/kg]
Ba	22	0.69
Cr	0.63	0.12
Cu	0.9	14
Mo	1	1.1
Sb	0.32	0.22
As	0.9	<0.05
Cd	0.04	<0.001
Co	0.54	<0.030
Pb	2.3	<0.1
Ni	0.44	0.24
Se	0.15	<0.007
Sn	0.4	<0.02
V	1.8	<0.1
Zn	4.5	0.48
Cl ⁻	616	6200
Br ⁻	20	–
F ⁻	55	2.4
SO ₄ ²⁻	2430	1700
pH	–	11.28

¹ The leaching limits imposed by the Soil Quality Decree (2007) for the use of granular material in the open/non-isolated environment.

² Column leaching test was performed in accordance with NEN 7383:2004.

able Sb in BA at a pH of 11.28 (Table 6). Due to the absence of Sb from F1, it can be speculated that immobilization of antimony occurred through the precipitation of new phases.

Although S contains approximately 5 times more Pb compared to the M fraction, the amount extracted from the two fractions was noted to be similar: 2 and 5 ppm, respectively. This indicates the presence of sparingly soluble Pb species in the bottom ash under these conditions. Additionally, the distribution of Pb in the mineral phases could not be confirmed using the PARC analysis because the concentrations were below the detection limit.

3.3.2. Reducible fraction (F2)

In the second step (F2) of the extraction, Fe-Mn oxyhydroxides were targeted in the reducing environment. In this step, the remaining weathering products (calcite, zeolite and gypsum) were dissolved from S and the partial dissolution of melilite, pyroxene and apatite was observed from the both fractions. The amorphous content of S and M was decreased by 5.7 and 9.7 wt%, respectively. Additionally, even after washing, the solid residues from F2 contained newly precipitated phases (ammonium chloride) from the extraction reagents.

The PTEs contents in the extraction solutions obtained during the F2 step is provided in Fig. 6. Although the percent content of Zn associated with the phases dissolved in F2 was similar for both fractions (30%), in terms of absolute content, the amount of Zn from S (3571 ppm) was more than double when compared to M (1540 ppm). Similarly, the content of Cu extracted from S was higher as compared to the M fraction. The incomplete dissolution of the weathering products in step F1 partially contributed to the higher release of Zn and Cu from S in this step but did not account for all of it.

During F2, comparable contents of Ni (S: 26 and M: 21 ppm), Cr (S: 23 and M: 27 ppm) and Pb (S: 63 and M: 79 ppm) were released in the extraction solutions, despite the fact that the absolute content of PTEs in S was significantly higher compared to M. In contrast to the previous extraction step, the supernatants from F2 showed the presence of low amounts of Sb (F: 1.3 and M: 3.26 ppm). As discussed earlier in Section 3.3.1, during F1 the absence of the Sb in the solution suggests the co-precipitation or

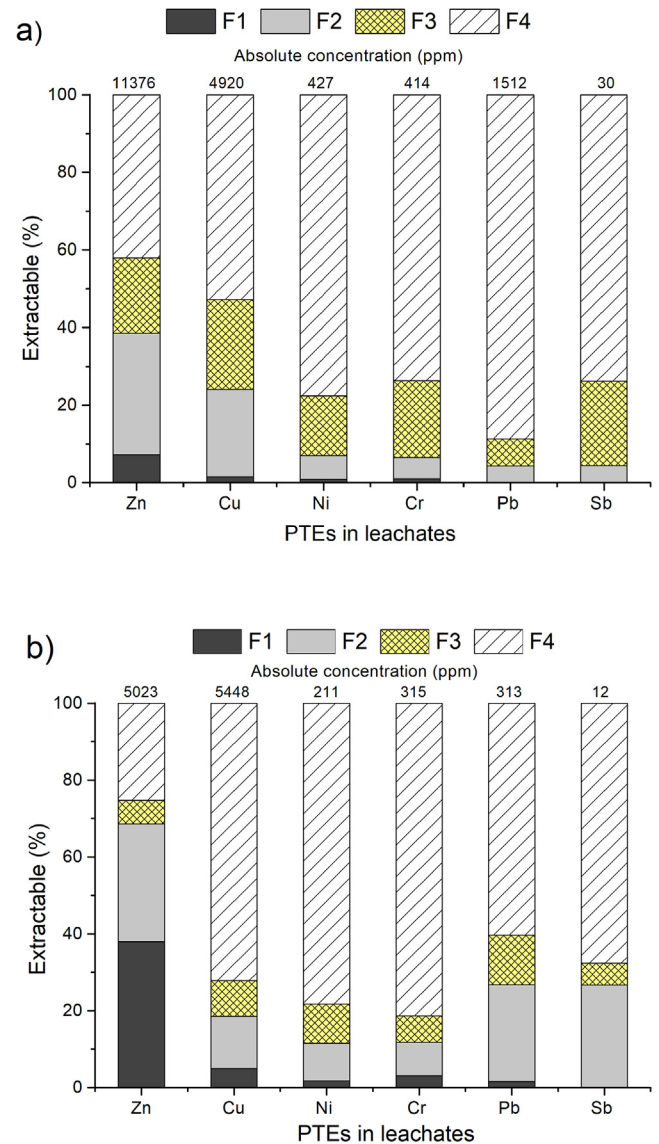


Fig. 6. Partition of Zn, Cu, Ni, Cr, Pb and Sb during different steps of sequential extraction in the (a) S (≤ 0.125 mm) and (b) M (0.125 – 1 mm) fractions of the MSWI bottom ash. F1: Exchangeable, F2: Reducible, F3: Oxidisable and F4: Inert fraction. The cumulative contents of PTEs (in ppm) extracted from all four steps of SEP are given at the top of every column for the respective element.

adsorption of the acid soluble fraction onto newly formed phases. The PTEs released during F2 can be associated with the amorphous Fe-Mn-oxyhydroxides that have been reported as a good sorbent for different transition and metals cations (Dijkstra et al., 2008; Meima and Comans, 1998).

3.3.3. Oxidizable fraction (F3)

Complexation of the PTEs with organic matter such as a fulvic and humic acid is a well-studied phenomenon (Arickx et al., 2007; Weng et al., 2002). In the case of BA, the leaching of numerous PTEs, i.e., Cu, Zn and Sb, was noted to have a correlation with the amount of organic matter (van Zomeren and Comans, 2004; Verbinen et al., 2016; Yao et al., 2012) and the F3 extraction step creates oxidizing conditions for its destruction. The TOC of the S and M fractions was similar: 2.68 and 2.71 wt%, respectively. The content of Zn (S: 2214, M: 304 ppm) and Cu (S: 1139, M: 508 ppm) released into the extraction solutions from F3 is illustrated in Fig. 6. Furthermore, in the case of S, increased contents

of Ni, Cr, Pb and Sb were observed in the extraction solutions from F3 as compared to F2 (Fig. 6a). For M a similar increase in the content of these elements occurred, with exception to Ni, which remained unchanged.

In addition to the TOC, other minerals such as melilite, plagioclase and spinel were also partially dissolved in F3. Melilite from the S fraction was completely dissolved because of the higher surface area of ash particles and the acidic environment, while in M only 0.7 wt% remained (Fig. 4a: bar S-F3). In the case of hematite, a slight increase in the contents was also observed for both fractions, while the total amorphous content remained almost unchanged.

3.3.4. Residual fraction (F4)

The residues obtained after F3 were digested with aqua regia for the determination of the residual content of the PTEs. During this step of the extraction, a significant amount of the crystalline and amorphous phases was dissolved (Fig. 5). It can be seen from Fig. 6 that a significant portion (40–80 wt%) of these PTEs were released in F4. The PTEs released during this extraction can be considered immobile because of their incorporation into silicates and other minerals with low solubility.

3.4. Comparison between SEP and PARC/XRD data

In order to calculate the theoretical content of PTEs that can be released in each sequential extraction step, the decrease in contents of minerals and amorphous phase after each SEP step was determined via the Rietveld method. The release of PTEs was then calculated based on the PARC determined composition of these phases (Table 1). However, PARC determined several different amorphous phases that could not be differentiated via XRD. Conversely, some phases were identified via XRD but not in PARC as discussed previously, meaning no information about the PTE content of these phases was available. Therefore, these phases were added to the amorphous content determined via XRD and the composition of this sum was then taken to be the average of all PARC phases that were not identified as a mineral via XRD (Section 3.1). The result of the calculation provides a semi-quantitative and theoretical concentration of PTEs released in each step.

By comparing the overall chemical composition of the BA determined via PARC and XRF (Table 5), it can be seen that PARC results overestimated the content of Ni by one order of magnitude. The Cr

content measured with the two methods was similar but was not considered further for the calculations due to its low concentration. PARC data about Sb was not available due to the spectral overlap between the Sb L_{α} and the Ca K_{α} lines. Therefore, the theoretical extractable contents of these elements were not calculated. In the case of Zn and Cu, their relatively high content and the good agreement between PARC and XRF values made them suitable candidates for calculating the theoretical content released during each step of SEP. Only the data from M is shown in Fig. 7, the S fraction followed a similar pattern which is provided in Appendix A (Fig. A5). During the extraction step F1, the extracted content of Cu was lower than the theoretically calculated value (Fig. 7b). This may indicate that the Cu released from dissolved phases was immobilized again via precipitation/sorption leading to differences between theoretical and measured contents. In the remaining extraction steps, the extracted content of Cu exceeded the calculated one significantly (Fig. 7). In the case of Zn, the extractable contents released during the extraction steps were always higher than the theoretically calculated contents. The calculated theoretical contents of Cu and Zn does not take the contents associated with organic matter and Fe-Mn-oxyhydroxides into account because these phases cannot be analyzed by using XRD/PARC. However, the chemical conditions of the extraction step F2 and F3 were designed for the dissolution of Fe-Mn-oxyhydroxides and organic matter, respectively. In Fig. 7, the contents of Zn and Cu in the extraction solutions of F2 and F3 are higher than the calculated values. This difference can be explained by the fact that the targeted phases were indeed present in the sample (F2: hydrous oxides and F3: organic matter) and that the extractions steps were partially effective in targeting their intended phases.

The results obtained with SEP provide validation for the conclusions drawn from the study of the phase composition. For example, the leaching of Zn during the column test from BA (≤ 4 mm) is minor (Table 6: 0.48 ppm) and the analysis of the phase composition indicated that most of the Zn content was associated with calcite. During the F1 extraction step, calcite was the intended target and the extracted solution showed the high content of Zn released in the solution. Based on the results obtained from the F2 and F3 extraction steps, it is also clear that SEP can provide indirect information about the PTE content associated with phases, such as Fe-Mn-oxyhydroxides and organic matter that cannot be detected via XRD or EDX/PARC. Although non-specificity of the SEP extrac-

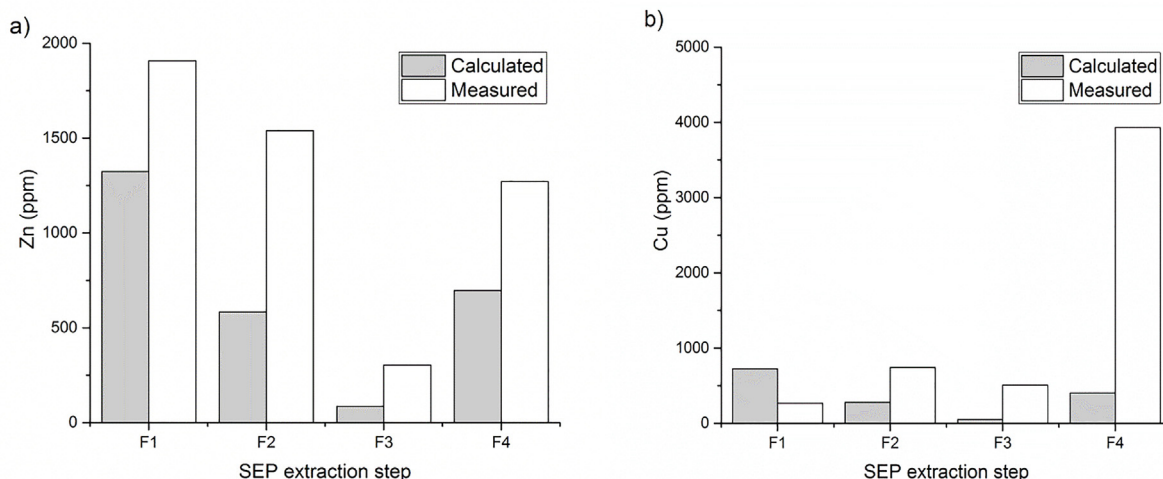


Fig. 7. Comparison between the measured and theoretically calculated concentration of (a) Zn and (b) Cu from each sequential extraction step performed on the M fraction. (F1: Exchangeable, F2: Reducible, F3: Oxidisable and F4: Inert fraction). Calculation for the theoretical concentrations is explained in Section 3.4.

tion step in targeting intended phases was observed, this effect can be taken into account with the knowledge of the changes in mineral composition after the extraction.

4. Conclusions and future prospects

- A novel multi-method approach using large area phase mapping/PARC and quantitative XRD was effective for analyzing a complex, heterogeneous material such as BA that contains many different crystalline and amorphous phases. However, it proved limited for the organic matter or phases below 1 μm in size. The microstructure of BA particles ≤ 4 mm consisted of a relatively homogenous core surrounded by an inhomogeneous layer containing smaller particles. This layer was produced by the phases formed during the incineration, quenching or weathering process. It was composed mostly of melilite and amorphous phases with a melilitic composition. The ratio of crystalline to amorphous was 1:2.
- Calcite, melilite and iron oxides contained the highest percentage of PTEs present in BA. The iron oxides: magnetite, hematite and wuestite contained a high percentage of Ni and Cu, while melilite appeared to incorporate a large percentage of PTEs (10–15% of Cr, Ni, Cu, Zn).
- The S fraction (≤ 0.125 mm) had a unique composition compared to the larger fractions, containing the weathering products, i.e., ettringite, gypsum and zeolite. This fraction was also the most contaminated one according to its overall chemical composition. Therefore, a potential treatment for the ≤ 4 mm BA could be the removal of the S fraction via dry or wet sieving, which could produce clean, recyclable aggregates for application in building materials.
- SEP data was used in combination with spectroscopic methods to complement the results regarding the association of PTEs with the mineral phases of BA. Furthermore, the PTEs contents associated with the phases that are challenging to observe with microanalyses e.g., organic matter and Fe-Mn-hydrous oxides, were investigated.
- According to SEP results, a high percentage (40–80 wt%) of each investigated PTE can be considered immobile and not susceptible to leaching in the environment.

4.1. Future prospects

- BCR sequential extraction protocol could be modified to discriminate better between the different phases of the bottom ash that is characterized by high alkalinity, carbonate and amorphous contents.
- In addition to mineralogical changes, quantifying the change in TOC content after each extraction step of the BCR sequential procedure is recommended to validate the findings of this study.

Conflict of interest

The authors declare no competing financial interest.

Acknowledgements

The authors would like to acknowledge the financial support provided by NWO (Nederlandse Organisatie voor Wetenschappelijk Onderzoek), the Netherlands, under the project number 10019729: “Environmental concrete based on the treated MSWI bottom ashes”. Special thanks to S. Melzer and P. Sturm for performing XRD and TOC measurements, respectively.

Appendix A. Supplementary material

Supplementary data to this article can be found online at <https://doi.org/10.1016/j.wasman.2019.01.031>.

References

- Alam, Q., Florea, M.V.A., Schollbach, K., Brouwers, H.J.H., 2017. A two-stage treatment for Municipal Solid Waste Incineration (MSWI) bottom ash to remove agglomerated fine particles and leachable contaminants. *Waste Manage.* 67, 181–192. <https://doi.org/10.1016/j.wasman.2017.05.029>.
- Alam, Q., Hendrix, Y., Thijs, L., Lazaro, A., Schollbach, K., Brouwers, H.J.H., 2018. Novel low temperature synthesis of sodium silicate and ordered mesoporous silica from incineration bottom ash. *J. Clean. Prod.* 211, 874–883. <https://doi.org/10.1016/j.jclepro.2018.11.173>.
- Alam, Q., Schollbach, K., Florea, M.V.A., Brouwers, H.J.H., 2016. Investigating washing treatment to minimize leaching of chlorides and heavy metals from MSWI bottom ash. 4th International Conference on Sustainable Solid Waste Management, Limassol, Cyprus.
- Arickx, S., Van Gerven, T., Boydens, E., L'hoest, P., Blanpain, B., Vandecasteele, C., 2008. Speciation of Cu in MSWI bottom ash and its relation to Cu leaching. *Appl. Geochem.* 23, 3642–3650. <https://doi.org/10.1016/j.apgeochem.2008.09.006>.
- Arickx, S., Van Gerven, T., Knaepkens, T., Hindrix, K., Evens, R., Vandecasteele, C., 2007. Influence of treatment techniques on Cu leaching and different organic fractions in MSWI bottom ash leachate. *Waste Manage.* 27, 1422–1427. <https://doi.org/10.1016/j.wasman.2007.03.015>.
- Bayuseno, A.P., Schmahl, W.W., 2010. Understanding the chemical and mineralogical properties of the inorganic portion of MSWI bottom ash. *Waste Manage.* 30, 1509–1520. <https://doi.org/10.1016/j.wasman.2010.03.010>.
- Bigham, J., Nordstrom, D., 2000. Iron and aluminum hydroxysulfates from acid sulfate waters. *Rev. Mineral. Geochem.* 40, 351–403.
- Bourtsalas, A., Vandeperre, L.J., Grimes, S.M., Themelis, N., Cheeseman, C.R., 2015. Production of pyroxene ceramics from the fine fraction of incinerator bottom ash. *Waste Manage.* 45, 217–225. <https://doi.org/10.1016/j.wasman.2015.02.016>.
- Bruder-Hubscher, V., Lagarde, F., Leroy, M.J.F., Coughanowr, C., Enguehard, F., 2002. Application of a sequential extraction procedure to study the release of elements from municipal solid waste incineration bottom ash. *Anal. Chim. Acta* 451, 285–295. [https://doi.org/10.1016/S0003-2670\(01\)01403-9](https://doi.org/10.1016/S0003-2670(01)01403-9).
- Caprai, V., Florea, M.V.A., Brouwers, H.J.H., 2017. Evaluation of the influence of mechanical activation on physical and chemical properties of municipal solid waste incineration sludge. *J. Environ. Manage.*, 1–12. <https://doi.org/10.1016/j.jenvman.2017.05.024>.
- Carpenter, M.A., 1994. Subsolidus phase relations of the plagioclase feldspar solid solution. In: Parsons, I. (Ed.), *Feldspars and Their Reactions*. Springer, Netherlands, Dordrecht, pp. 221–269. https://doi.org/10.1007/978-94-011-1106-5_6.
- Chen, C.-H., Chiou, I.-J., 2007. Distribution of chloride ion in MSWI bottom ash and de-chlorination performance. *J. Hazard. Mater.* 148, 346–352. <https://doi.org/10.1016/j.jhazmat.2007.02.046>.
- Chiang, Y.W., Santos, R.M., Vanduyfhuys, K., Meesschaert, B., Martens, J.A., 2014. Atom-efficient route for converting incineration ashes into heavy metal sorbents. *ChemSusChem* 7, 276–283. <https://doi.org/10.1002/cssc.201300704>.
- Chimenos, J., Segarra, M., Fernández, M., Espiell, F., 1999. Characterization of the bottom ash in municipal solid waste incinerator. *J. Hazard. Mater.* 64, 211–222. [https://doi.org/10.1016/S0304-3894\(98\)00246-5](https://doi.org/10.1016/S0304-3894(98)00246-5).
- Chimenos, J.M., Fernández, A., Nadal, R., Espiell, F., 2000. Short-term natural weathering of MSWI bottom ash. *J. Hazard. Mater.* 79, 287–299. [https://doi.org/10.1016/S0304-3894\(00\)00270-3](https://doi.org/10.1016/S0304-3894(00)00270-3).
- Coelho, A.A., 2018. TOPAS and TOPAS-Academic: an optimization program integrating computer algebra and crystallographic objects written in C++. *J. Appl. Crystallogr.* 51, 210–218. <https://doi.org/10.1107/S1600576718000183>.
- Cornelis, G., Van Gerven, T., Vandecasteele, C., 2005. The effect of calcium-bearing minerals on the solubility of molybdate and antimonate in alkaline wastes. *International Conference on Engineering for Waste Treatment*, Albi, France.
- Davidson, C.M., Gibson, M.D., Hamilton, E., MacGillivray, B.H., Reglinski, J., Rezabal, E., 2005. The long-term environmental behaviour of strontium and barium released from former mine workings in the granites of the Sunart region of Scotland, UK. *Chemosphere* 58, 793–798. <https://doi.org/10.1016/j.chemosphere.2004.08.101>.
- Deer, W.A., Howie, R.A., Zussman, J., 1997. *Rock-forming minerals*, Vol. 2A. Single-chain silicates. Geological Society.
- Deer, W.A., Howie, R.A., Zussman, J., 1986. *Rock-Forming Minerals - Disilicates and Ring Silicates*.
- Dijkstra, J.J., Meeussen, J.C.L., Van der Sloot, H.A., Comans, R.N.J., 2008. A consistent geochemical modelling approach for the leaching and reactive transport of major and trace elements in MSWI bottom ash. *Appl. Geochem.* 23, 1544–1562. <https://doi.org/10.1016/j.apgeochem.2007.12.032>.
- Dijkstra, J.J., van der Sloot, H.A., Comans, R.N.J., 2006. The leaching of major and trace elements from MSWI bottom ash as a function of pH and time. *Appl. Geochem.* 21, 335–351. <https://doi.org/10.1016/j.apgeochem.2005.11.003>.
- Directive 2000/76/EC, 2000. Directive 2000/76/EC on the Incineration of Waste. *Off. J. Eur. L* 332, 91–111.

- Eighmy, T.T., Eusden, J.D., Marsella, K., Hogan, J., Domingo, D., Krzanowski, J.E., Stämpfli, D., 1994. Particle petrogenesis and speciation of elements in MSWI bottom ashes. *Stud. Environ. Sci.* 60, 111–136. [https://doi.org/10.1016/S0166-1116\(08\)71452-3](https://doi.org/10.1016/S0166-1116(08)71452-3).
- EU Commission, 2014. Towards a circular economy: a zero waste programme for Europe.
- Eusden, J.D., Eighmy, T.T., Hockert, K., Holland, E., Marsella, K., 1999. Petrogenesis of municipal solid waste combustion bottom ash. *Appl. Geochem.* 14, 1073–1091. [https://doi.org/10.1016/S0883-2927\(99\)00005-0](https://doi.org/10.1016/S0883-2927(99)00005-0).
- Gougar, M.L.D., Scheetz, B.E., Roy, D.M., 1996. Ettringite and C-S-H Portland cement phases for waste ion immobilization: a review. *Waste Manage.* 16, 295–303. [https://doi.org/10.1016/S0956-053X\(96\)00072-4](https://doi.org/10.1016/S0956-053X(96)00072-4).
- Greendeal-GD076, 2012. Greendeals GD076: sustainable useful application of WtE bottom ash [WWW Document]. Dutch Minist. Infrastruct. Environ. URL <<http://www.greendeals.nl/gd076-verduurzaming-nuttige-toepassing-aec-bodemassen/>> (accessed 8.9.16).
- Gualtieri, A.F., 2000. Accuracy of XRPD QPA using the combined Rietveld–RIR method. *J. Appl. Crystallogr.* 33, 267–278. <https://doi.org/10.1107/S002188989901643X>.
- Hampsoim, C.J., Bailey, J.E., 1982. On the structure of some precipitated calcium aluminosulphate hydrates. *J. Mater. Sci.* 17, 3341–3346. <https://doi.org/10.1007/BF01203504>.
- Hendrix, Y., Alam, Q., Thijs, L., Lazaro, A., Brouwers, H.J.H., 2017. Green synthesis of water-glass from municipal solid waste incineration bottom ash. In: *The 9th International Symposium on Cement and Concrete (ISCC 2017)*, Wuhan, China, pp. 1–4.
- Hughes, J.M., Rakovan, J., 2002. The crystal structure of apatite, $\text{Ca}_5(\text{PO}_4)_3(\text{F}, \text{OH}, \text{Cl})$. *Rev. Mineral. Geochem.* 48, 1 LP–12.
- Lakshmanan, L.Z., Stipp, S.L.S., 2007. Experimental study of nickel(II) interaction with calcite: adsorption and coprecipitation. *Geochim. Cosmochim. Acta* 71, 3686–3697. <https://doi.org/10.1016/j.gca.2007.04.006>.
- Landsberger, S., Buchholz, B.A., Kaminski, M., Plewa, M., 1993. Trace elements in municipal solid waste incinerator fly ash. *J. Radioanal. Nucl. Chem. Artic.* 167, 331–340. <https://doi.org/10.1007/BF02037191>.
- Meima, J.A., Comans, R.N.J., 1998. Application of surface complexation/precipitation modeling to contaminant leaching from weathered municipal solid waste incinerator bottom ash. *Environ. Sci. Technol.* 32, 688–693. <https://doi.org/10.1021/es9701624>.
- Nirel, P.M.V., Morel, F.M.M., 1990. Pitfalls of sequential extractions. *Water Res.* 24, 1055–1056. [https://doi.org/10.1016/0043-1354\(90\)90129-T](https://doi.org/10.1016/0043-1354(90)90129-T).
- Osborn, E.F., Schairer, J.F., 1941. The ternary system pseudowollastonite–akermanite–gehlenite. *Am. J. Sci.* 239, 715–763. <https://doi.org/10.2475/ajs.239.10.715>.
- Palmer, L.C., Newcomb, C.J., Kaltz, S.R., Spoerke, E.D., Stupp, S.I., 2008. Biomimetic systems for hydroxyapatite mineralization inspired by bone and enamel. *Chem. Rev.* 108, 4754–4783. <https://doi.org/10.1021/cr8004422>.
- Penilla, R.P., Bustos, A.G., Elizalde, S.G., 2003. Zeolite synthesized by alkaline hydrothermal treatment of bottom ash from combustion of municipal solid wastes. *J. Am. Ceram. Soc.* 86, 1527–1533. [https://doi.org/10.1151-2916.2003.tb03509.x](https://doi.org/10.1111/j.1151-2916.2003.tb03509.x).
- Piantone, P., Bodénan, F., Chatelet-Snidaro, L., 2004. Mineralogical study of secondary mineral phases from weathered MSWI bottom ash: implications for the modelling and trapping of heavy metals. *Appl. Geochem.* 19, 1891–1904. <https://doi.org/10.1016/j.apgeochem.2004.05.006>.
- Pöllmann, H., 2010. Mineralisation of Wastes and Industrial Residues. Shaker Verlag, Aachen.
- Railsback, L.B., 1999. Patterns in the compositions, properties, and geochemistry of carbonate minerals. *Carbonates Evaporites* 14, 1. <https://doi.org/10.1007/BF03176144>.
- Rauret, G., López-Sánchez, J.F., Sahuquillo, A., Rubio, R., Davidson, C., Ure, A., Quevauviller, P., 1999. Improvement of the BCR three step sequential extraction procedure prior to the certification of new sediment and soil reference materials. *J. Environ. Monit.* 1, 57–61. <https://doi.org/10.1039/a807854h>.
- Schollbach, K., Alam, Q., Caprai, V., Florea, M.V.A., Van der Laan, S.R., Van Hoek, C.J.G., Brouwers, H.J.H., 2016. Combined characterization of the MSWI bottom ash. In: *Proceedings of the Thirty-Eighth International Conference on Cement Microscopy*, pp. 74–84.
- Soil Quality Decree, 2007. Regeling Bodemkwaliteit, VROM, Den Haag: Ruimte en Milieu. Ministerie van Volkshuisvesting, Ruimtelijke Ordening en Milieubeheer.
- Speiser, C., Baumann, T., Niessner, R., 2001. Characterization of municipal solid waste incineration (MSWI) bottom ash by scanning electron microscopy and quantitative energy dispersive X-ray microanalysis (SEM/EDX). *Fresenius J. Anal. Chem.* 370, 752–759. <https://doi.org/10.1007/s002160000659>.
- Sulkowski, M., Hirner, A.V., 2006. Element fractionation by sequential extraction in a soil with high carbonate content. *Appl. Geochem.* 21, 16–28. <https://doi.org/10.1016/J.APGEOCHEM.2005.09.016>.
- Teichert, G., Strohmman, R., Paufler, P., Schreiter, P., 1982. On the Density of Synthetic Glasses in the System Soda Melilite – Gehlenite/Akermanite. *Cryst. Res. Technol.* 17, 891–895. <https://doi.org/10.1002/crat.2170170716>.
- Van Caneghem, J., Verbinen, B., Cornelis, G., de Wijs, J., Mulder, R., Billen, P., Vandecasteele, C., 2016. Immobilization of antimony in waste-to-energy bottom ash by addition of calcium and iron containing additives. *Waste Manage.* 54, 162–168. <https://doi.org/10.1016/j.wasman.2016.05.007>.
- van Hoek, C.J.G., Small, J., van der Laan, S.R., 2016. Large area phase mapping using PhAse Recognition and Characterization (PARC) software. *Micros. Today* 24.
- van Zomeren, A., Comans, R.N.J., 2004. Contribution of natural organic matter to copper leaching from municipal solid waste incinerator bottom ash. *Environ. Sci. Technol.* 38, 3927–3932. <https://doi.org/10.1021/es035266v>.
- Verbinen, B., Billen, P., Vandecasteele, C., 2014. Thermal treatment of solid waste in view of recycling: Chromate and molybdate formation and leaching behaviour. *Waste Manage. Res.* 32, 536–542. <https://doi.org/10.1177/0734242X14532004>.
- Verbinen, B., Van Caneghem, J., Billen, P., Vandecasteele, C., 2016. Long term leaching behavior of antimony from MSWI bottom ash: influence of mineral additives and of organic acids. *Waste Biomass Valorization* 1–8. <https://doi.org/10.1007/s12649-016-9796-6>.
- Wei, Y., Mei, X., Shi, D., Liu, G., Li, L., Shimaoka, T., 2017. Separation and characterization of magnetic fractions from waste-to-energy bottom ash with an emphasis on the leachability of heavy metals. *Environ. Sci. Pollut. Res.* 24, 14970–14979. <https://doi.org/10.1007/s11356-017-9145-8>.
- Wei, Y., Shimaoka, T., Saffarzadeh, A., Takahashi, F., 2011. Mineralogical characterization of municipal solid waste incineration bottom ash with an emphasis on heavy metal-bearing phases. *J. Hazard. Mater.* 187, 534–543. <https://doi.org/10.1016/j.jhazmat.2011.01.070>.
- Weng, L., Temminghoff, E.J.M., Lofts, S., Tipping, E., Riemsdijk, W.H. Van, 2002. Complexation with dissolved organic matter and solubility control of heavy metals in a sandy soil complexation with dissolved organic matter and solubility control of heavy metals in a sandy soil. *Environ. Sci. Technol.* 36, 4804–4810. <https://doi.org/10.1021/es0200084>.
- Wiedenmann, D., Zaitsev, A.N., Britvin, S.N., Krivovichev, S.V., Keller, J., 2009. Alumoakermanite, $(\text{Ca}, \text{Na})_2(\text{Al}, \text{Mg}, \text{Fe}^{2+})(\text{Si}_2\text{O}_7)$, a new mineral from the active carbonatite–nephelinite–phonolite volcano Oldoinyo Lengai, northern Tanzania. *Mineral. Mag.* 73, 373–384. <https://doi.org/10.1180/minmag.2009.073.3.373>.
- Wiles, C.C., 1996. Municipal solid waste combustion ash: state-of-the-knowledge. *J. Hazard. Mater.* 47, 325–344. [https://doi.org/10.1016/0304-3894\(95\)00120-4](https://doi.org/10.1016/0304-3894(95)00120-4).
- Yao, J., Li, W.-B., Kong, Q.-N., Wu, Y.-Y., He, R., Shen, D.-S., 2010. Content, mobility and transfer behavior of heavy metals in MSWI bottom ash in Zhejiang province, China. *Fuel* 89, 616–622. <https://doi.org/10.1016/j.fuel.2009.06.016>.
- Yao, J., Li, W.-B., Kong, Q., Xia, F., Shen, D.-S., 2012. Effect of weathering on the mobility of zinc in municipal solid waste incinerator bottom ash. *Fuel* 93, 99–104. <https://doi.org/10.1016/j.fuel.2011.11.026>.
- Yu, J., Sun, L., Xiang, J., Jin, L., Hu, S., Su, S., Qiu, J., 2013. Physical and chemical characterization of ashes from a municipal solid waste incinerator in China. *Waste Manage. Res.* 31, 663–673. <https://doi.org/10.1177/0734242X13485793>.
- Zevenbergen, C., Wood, T., Vander, Bradley, J.P., Van Der Broeck, P.F.C.W., Orbons, A. J., Van Reeuwijk, L.P., 1994. Morphological and chemical properties of MSWI bottom ash with respect to the glassy constituents. *Hazard. Waste Hazard. Mater.* 11, 371–383. <https://doi.org/10.1089/hwm.1994.11.371>.